3D direct printing of mechanical and biocompatible hydrogel meta-structures

Lei Zhang [a,b,1], Wenhan Lee [c,1], Xinhao Li [d], Yanhui Jiang [a], Nicholas Xuanlai Fang [d], Guohao Dai [c,**], Yongmin Liu [a,e,*]

[a] Department of Mechanical & Industrial Engineering, Northeastern University, Boston, MA, 02115, United States
[b] State Key Laboratory of Primate Biomedical Research, Institute of Primate Translational Medicine, Kunming University of Science and Technology, Kunming, 650500, China
[c] Department of Bioengineering, Northeastern University, Boston, MA, 02115, United States
[d] Department of Mechanical Engineering, Massachusetts Institute of Technology, Cambridge, MA, 02139, United States
[e] Department of Electrical and Computer Engineering, Northeastern University, Boston, MA, 02115, United States

A R T I C L E   I N F O

A B S T R A C T

Direct Ink Writing (DIW) has demonstrated great potential as a versatile method to 3D print multifunctional structures. In this work, we report the implementation of hydrogel meta-structures using DIW at room temperature, which seamlessly integrate large specific surface areas, interconnected porous characteristics, mechanical toughness, biocompatibility, and water absorption and retention capabilities. Robust but hydrophobic polymers and weakly crosslinked nature-origin hydrogels form a balance in the self-supporting ink, allowing us to directly print complex meta-structures without sacrificial materials and heating extrusion. Mechanically, the mixed bending or stretching of symmetrical re-entrant cellular lattices and the unique curvature patterns are combined to provide little lateral expansion and large compressive energy absorbance when external forces are applied on the printed meta-structures. In addition, we have successfully demonstrated ear, aortic valve conduits and hierarchical architectures. We anticipate that the reported 3D meta-structured hydrogel would offer a new strategy to develop functional biomaterials for tissue engineering applications in the future.

1. Introduction

Naturally derived hydrogel inks, like Alginate, in combination with 3D printing technique promise many applications in tissue engineering, drug delivery and cell encapsulation for the practice of personalized customization [1–5]. Hydrogel biomaterials are highly biocompatible and flexible, because of their high water content arising from the hydrophilic functional groups and the interwoven structures that imitate the natural extracellular matrix (ECM). These unique properties can provide a favorable environment for cellular and biological factor permissive behavior [6,7]. Direct Ink Writing (DIW) has demonstrated great potential as a versatile method to 3D print multifunctional structures. The integration of computer-aided design (CAD) and rapid prototyping endows DIW the ability to produce the structures with overall size and shape, pore size, shape, interconnection, and distribution control of highly complex biomedical devices [8]. However, the hydrogel ink has limitations to achieve both excellent DIW 3D printability (especially direct printing at room temperature without supporting sacrificial materials or UV irradiation curing) and desired functionality including mechanical toughness.

DIW of 3D structures requires that inks can "flow" as a liquid during extrusion and "freeze" as a solid after extrusion. Without supporting sacrificial materials or curing methods, it is very difficult to print naturally derived Alginate hydrogel into complex structures, while possessing robust mechanical and biocompatibility [9–12]. To mechanically reinforce Alginate hydrogel, many effective approaches [13–15] have been developed via hybrid printing of thermoplastic polymers (biodegradable polymers) such as polycaprolactone (PCL) and

copolymer poly (glycolic) acid (PLGA) filaments. The whole scaffold can be significantly reinforced using the separate PCL frame but little mechanical interactions exist at the boundary between the PCL component and the hydrogel network, resulting in mechanical disintegration of the scaffold upon physiological loads [16,17]. Moreover, the large swelling-shrinking compatibility of hydrogel would further give rise to mechanical disintegration, and then to structure disintegration. Last but not the least, many 3D printed thermoplastic polymer filaments need to be heated to the melting temperature of approximately 100 °C to facilitate extrusion. The printing process is therefore generally slow, and some polymers undergo brittle transition [18].

In this work, we describe a self-supporting hydrogel ink to seamlessly integrate the mechanical toughness and 3D printability of DIW scaffolds at room temperature, without extra sacrificial materials or UV irradiation curing. The ink based on nano-composites imparts water absorption and retention capability, biocompatibility, mechanical toughness, as well as superior DIW 3D printability. Our method could be generalized to produce a wide combination of weakly crosslinked nature-origin hydrogel and biomedical thermoplastic polymers. To demonstrate the 3D printability, we show that a single nozzle can readily print human ear, human aortic valve conduits and 3D hierarchical structure with tunable infill density and infill pattern by accumulating the ink. In addition, we have printed and characterize Gyroid meta-structures, which exhibit unique properties such as light weight, large specific surface areas, interconnected porous characteristics, and mechanical robustness. It is shown that the nature-inspired cellular meta-structures printed with the functional ink generate substantial compressive energy absorbance, excellent water absorption and retention capability, and bioactivity. Our printed hydrogel meta-structures could be used in multiple areas, including tissue engineering, drug delivery system, molecular filters and superabsorbent devices.

2. Results and discussion

2.1. APH ink design and DIW 3D printability

As discussed previously, one of the major limitations of hydrogel-based 3D printing inks is that they are often mechanically weak, and hard to achieve the desired 3D printability. The FDA-approved thermoplastic biopolymers, such as PCL and PLGA, are promising materials for tissue repair, as they have advantages of stable mechanical strength, low cost and tunable biodegradation rate. However, they are bio-inert materials, and bi-layered printing of PCL frame and weak crosslinked hydrogel leads to mechanical disintegration, particularly at the high strains. To overcome the limits of hydrogel inks, we endow the weak crosslinked hydrogel ink integrated mechanical toughness, bioactivity, water absorption and desired 3D printability. We show that a single nozzle can directly print various thickened or curved 3D patterns with designed characteristics by accumulating the hydrogel inks at room temperature.

Fig. 1A presents a schematic summary of the synthesis and printability of the Alginate-PCL-HA (APH) ink. The detailed experimental procedures are described in Section A of Supplementary Materials. Briefly, a mixed precursor solvent of dichloromethane (DCM) and dibutyl phthalate (DBP) was used to dissolve polycaprolactone (PCL) pellets and make PCL liquid encapsulate with hydroxyapatite (HA) nano bioceramic homogeneously. Because the instinctive mechanical properties of the DIW structures strongly depend on the compositions of polymer and ceramic, herein an appropriate content ratio of the PCL and HA in the synthesized ink has been investigated. From the microstructure evolution images of primeval ink taken by a scanning electron microscope (SEM), the ideal ratio status is that the robust PCL can wrap ceramic agglomerate particles and then present whole plastic behavior under *in situ* stretching (see Section B and Fig. S1 in Supplementary Materials).

Under ambient conditions, DCM solvent has a high vapor pressure exceeding 50 kPa. The high vapor pressure of DCM results in rapid evaporation, hence it requires a large extrusion pressure and a strict
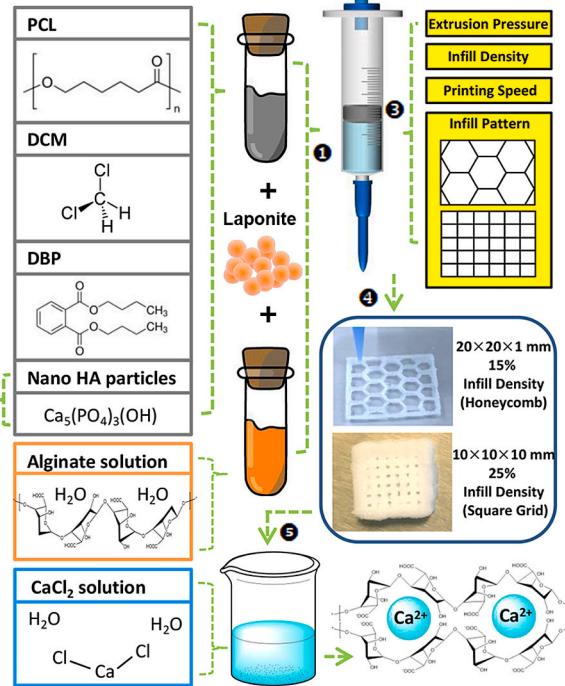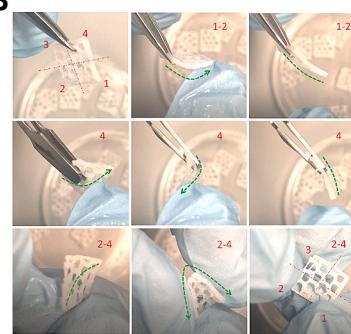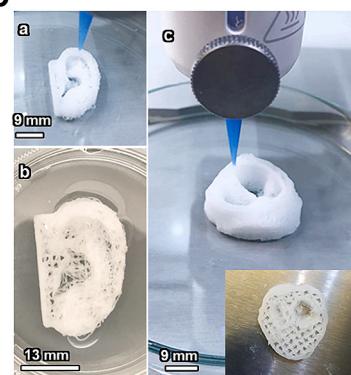
Fig. 1. Schematic summary of the synthesis and 3D printability of the APH ink. A: Illustration and demonstration of the synthesis the APH ink. The hydrophobic PCL and non-crosslinked Alginate aqueous solution together with HA ceramic produces a homogeneous balance in the ink (see also Supplementary Materials Fig. S3). B: Typical plate sample with honeycomb pattern that was bended along different directions (red number: 1, 2, 3 and 4). The DIW samples exhibited mechanical integrity and recovery capability before the ultimate strain. C: Scalable, customized and gradient implants, including human ear (a and b) and aortic valve conduits (c), which are directly printed from the APH ink. (For interpretation of the references to colour in this figure legend, the reader is referred to the Web version of this article.)

storage condition to maintain the ideal extrusion state of the ink. As a result, some researches [19,20] extruded the PCL filament under ambient conditions by adding DCM organic reagent that controls the viscosity. In this work, we use Laponite nanoclay ($Na^+_{0.7}$ $[(Si_8Mg_{5.5}Li_{0.3})O_{20}(OH)_4]^{-0.7}$) instead of the excess DCM [21], whose dual ionic characteristics can interact with guluronic and mannuronic acid groups in Alginate aqueous solution, to establish a relatively stable viscosity value of APH ink to ensure the continuous extrusion and the superior 3D printability. Moreover, degradation elements of Laponite play an important role in mediating cellular attachment, and exhibit a positive influence on bone metabolism and calcification [22,23].

Thermogravimetric analysis (TGA) profile is presented in Fig. S2 in Supplementary Materials. It reveals that APH scaffold contained about 5 wt % residual DCM solvents. The residual solvent can be removed through evaporation or rinsing with 75% ethanol. The incorporation of ceramics may increase the decomposition temperature of PCL. The TGA results validate that the final printed samples contain ceramics, and the ceramics do not decompose from room temperature to 600 °C. The hydrophobicity of PCL has a large contrast with the hydrophilicity of Alginate aqueous solution, which makes it difficult to be optimized into the homogenous ink. Incorporation of Laponite nanoclay into the APH network can provide an "intermediation" between hydrophobic PCL solvent and Alginate aqueous solution, which promotes the homogeneous composite ink with an ideal extrusion capacity (see Fig. S3 in Supplementary Materials), while regulating a balance between plasticity and elasticity. We have used the APH ink to print simple plates with different dimensions and patterns (*e.g.*, square grid and honeycomb) as shown in Fig. 1A❸ and ❹ (see also Movie S1 and S2 for the printing process). Microscopically (see Section B and Fig. S1 in Supplementary Materials), a suitable proportion of ink could make liquid PCL resemble a robust "skin" to tightly attach on the brittle bioceramic particles while maintain a rough surface. The robust "skin" helps the ink to enhance the mechanical toughness and the rough surface is favorable for the cell's adhesion. As a result, the printed samples present mechanical integrity and plastic behavior (Fig. 1B), besides the performance of homogeneous compositions and easy extrusion. As seen in Supplementary Materials Fig. S4, APH ink was directly extruded into 20 × 20 mm scaffold with square grid pattern infilled, according to the CAD structure input (Fig. S4A). The hydrogel scaffold presented the intersectional filaments and formed grid porous structures, as verified by optical photographs and SEM images (Fig. S4B). Incorporation of Laponite nanoclay into the APH network provided more mechanical support to maintain pore integrity. However, during the DIW process, the filament expanded upon deposition onto the platform due to the extrusion stress between nozzle and platform, thereby creating filaments that were slightly wider in width than in diameter. The expansion extent of the extrusion filament can be described as a ratio of the filament diameter and the nozzle diameter (22G), which was estimated to be 1.16 [24]. The increased Laponite particles in APH ink would make the ink undergo larger extrusion stress with a smaller layer thickness, thereby making the expansion of the width and diameter less significant.

In addition, the APH ink can be rapidly 3D-printed into scalable, complex, customized implants at a linear 3D-printing speed as high as 10–35 mm/s with a relatively low extrusion pressure of 15–180 psi and filamentary diameter of ~260 μm. Some examples include 35% large of human ear with 25% infill density (Fig. 1C(a) and Movie S3), 50% large of human ear with 15% infill density (Fig. 1C(b)) and human aortic valve conduits with 15% infill density (Fig. 1C(c) and Movie S4). The Alginate-based hydrogel with encapsulation of PCL thermoplastic polymer and HA ceramic maintains from 2D geometry to 3D structure and mechanical integrity after extrusion and crosslinking.

The DIW 3D printability in a highly reproducible and predictable manner further enables us to print 3D hierarchical structures with varying layer thicknesses using a single nozzle. During the printing, we fixed the printing parameters, including printing speed (15 mm/s), infill pattern and infill density (25%), while changing the extrusion pressure

only. The pore size and the density of plane samples were changed as we gradually increased the extrusion pressure (Fig. 2A). A similar printing behavior was developed for 3D hierarchical samples (Fig. 2B). The large extrusion pressure produced a denser and lower porosity basement structure, and the upper-structure with a higher porosity as well as larger pore size was directly printed by decreasing the extrusion pressure gradually (Fig. 2C). The 3D printability of APH ink was initially evaluated through shear viscosity measurement (AR-G2 Rheometer), as depicted in the left panel of Fig. 2D. It clearly shows that APH ink exhibits a strong shear-thinning behavior, which is an important requirement for DIW technique. During DIW, the ink needs to flow as a liquid during extrusion and then solidify after extrusion. A high viscosity impedes the surface-tension-driven droplet formation and the collapse of the printed structure. Next, we used oscillatory shear tests to analyze the viscoelastic behavior of the APH inks, as shown in the right panel of Fig. 2D. At low strain, the storage modulus (G′) and the loss modulus (G″) for APH inks are constant and parallel and G′ > G″, indicating that the ink is in a stable gel state with predominant elasticity. As the strain increases, the loss modulus G″ exceeds the shear storage modulus G′, and then the flow point is observed, indicating the transition initiation of the ink from solid-like to liquid-like behavior. Clearly, as Laponite increases from 0 to 10 wt%, the APH ink turns to gel-state at different strain. The strong shear-thinning behavior allows the APH ink to flow through the single nozzle tip easily and solidify as the stable structure after extrusion in the air (see also Movie S1- S4 for the printing process).

Next, to further test the 3D printability of our APH ink, we demonstrate complex Gyroid cellular meta-structural hydrogel without using supporting materials and extra curing methods. Gyroids belong to the triply periodic minimal surfaces (TPMS) topology, which are free of discontinuities or self-intersecting elements. They can be mathematically designed using level-set approximation technique [25]. A level-set approximation to the Gyroid is given by Refs. [26,27]:

$$\sin\frac{(2\pi x)}{a}\cos\frac{(2\pi y)}{a} + \sin\frac{(2\pi y)}{a}\cos\frac{(2\pi z)}{a} + \sin\frac{(2\pi z)}{a}\cos\frac{(2\pi x)}{a} = t \tag{1}$$

Here x, y, and z are the Cartesian coordinates, a is the periodicity of the Gyroid, and t is the level-set constant. It should be noted that the geometrical characteristics of TPMS are very distinct. A minimal surface is inherently smooth, without sharp edges or corners. In addition, it can split the space into two or more non-intersecting and intertwined domains that can be repeated periodically in three orthogonal directions (Fig. 3A). There exists competition between the forces of air on two sides of a curved wall, which makes the lattices wall prone to yield with the conjoint wall-to-wall contraction or densification. For these unique topological features, it is rather challenging to directly print Gyroid structures without extra supporting materials or UV radiation curing.

Using the APH ink, we have printed the Gyroid sheet-based structure at a linear 3D-printing speed of 15 mm/s with the extrusion pressure around 80 psi (Fig. 3B and Movie S5 for the printing process). Macroscopically, the extrusion printed scaffolds well resemble the Gyroid CAD model, which can be seen from both the front view and the isometric view with helically curved sheet features (Fig. 3C). The sheet size and pore core diameter of the as-printed samples vary from 1.83 to 2.94 mm (printed with 22 G nozzle) to 0.96 and 1.16 mm (printed with 27 G nozzle). In the Gyroid lattices, the forces from air on two sides of a curved wall compete with each other. If there is no air beneath the surface, then the air on top would push the surface down and vice versa. As a result, the lattice is in an equilibrium state, which makes Gyroid attractive and interesting on tissue engineering applications [28,29]. Our results strongly support the 3D printability of APH ink with good fidelity for mathematically defined architectures. Moreover, the ability to synthesize and 3D print APH inks with mechanical integrity under ambient conditions with no need for further sintering enables incorporation of biofunctional factors and protein molecules to take advantage of natural hydrogel in drug-loading and delivery [30].
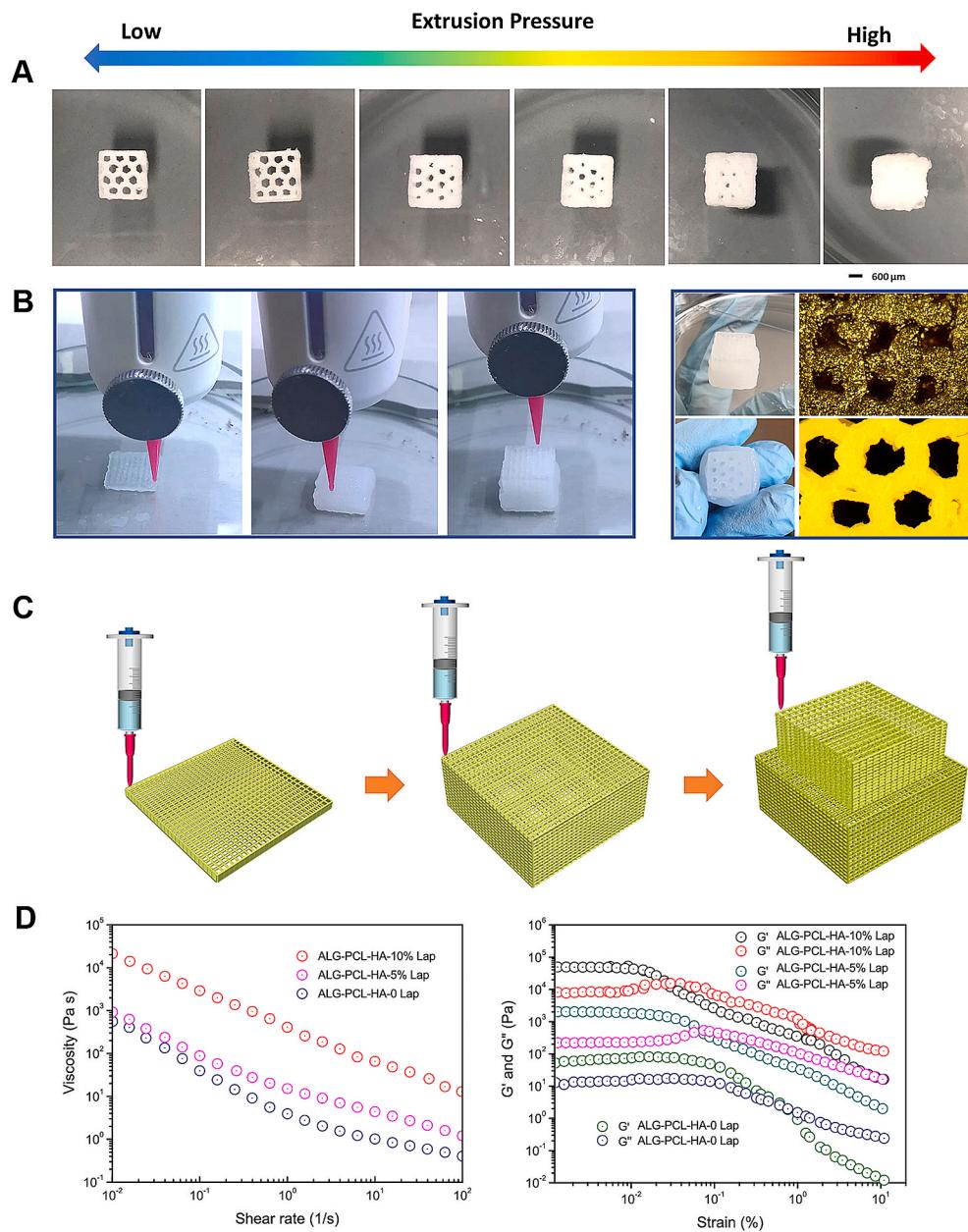
Fig. 2. A: Photograph series showing the pore characteristics of the samples (10 × 10 × 3 mm^3, honeycomb infill pattern and 25% infill density) that were printed with different extrusion pressures. B: Photograph series (left panel) showing that gradually adjusting the extrusion pressure can make a 3D hierarchical structure, either with square grid pattern or honeycomb pattern (right panel). C: Schematic illustration of the hierarchical printing process from the bottom (12.5 × 12.5 × 12.5 mm^3, 25% infill density) to top (10 × 10 × 10 mm^3, 25% infill density). D: The rheological characteristic of APH ink with different content of Laponite. Left: Log-log plot of viscosity (Pa·s) as a function of shear rate (1/s) for APH ink. Right: Log-log plot of shear storage (G′) and shear loss (G″) modulus (Pa) as a function of shear strain for the APH ink.
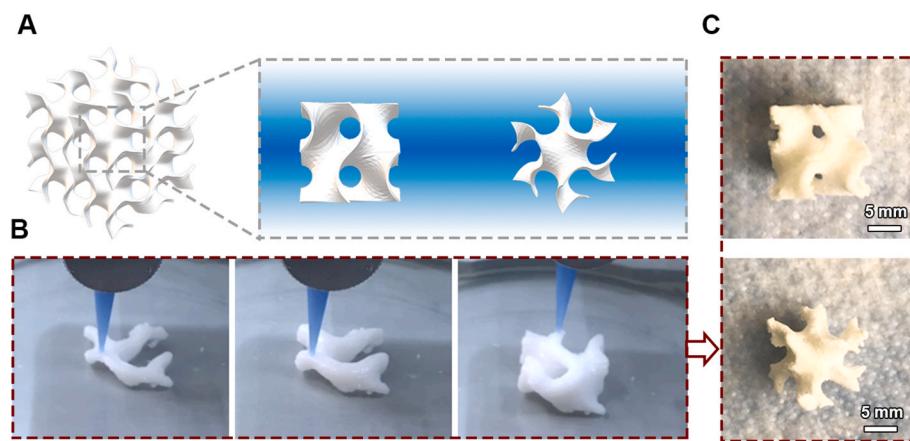

Fig. 3. DIW of Gyroid sheet-based structure in air. A: 4 × 4 Gyroid schematic structure in the isometric view. The right panel illustrates the unit cell in the front view and in the isometric view. The unique topological features make the lattices curved sheet prone to yield by gravity. However, the Gyroid structure can be directly printed using APH via single nozzle (B and C), without sacrificial/supporting materials beneath the periodical curved sheet (indicated by the red arrows). B: DIW process of Gyroid. C: Photographs of the printed Gyroid in the front view (top) and the isometric view (bottom). (For interpretation of the references to colour in this figure legend, the reader is referred to the Web version of this article.)

2.2. Mechanical property of printed samples

To experimentally demonstrate the structural-mechanical integration, the mechanical properties of the APH Gyroid were investigated by compression test (Fig. 4), from which we observed the enhanced mechanical performance arising from the unique characteristics of symmetrical curvature re-entrant structure in the APH DIW Gyroid sample. Square grid structures (Fig. 4A(a)), printed with the same volume of APH ink as the Gyroid samples (Fig. 4A(b)), were tested as a comparison. The compressive response of the square grid scaffold and the Gyroid scaffold were recorded by a digital video camera (see Movie S6 and Movie S7, respectively). The compression test of bulk sample made of APH ink was also conducted as the reference. Fig. 4B(a) displays the nominal stress-strain responses of the tested APH hydrogels with different structures. The hydrogels showed smooth deforming response, which resembles the typical nonlinear polymeric behaviors. The compressive stress-strain curve starts with an initial deformation and reaches a long deformation plateau close up to ~60% strain, indicating good ductility. After the plateau region, the curves enter the densification region where stress increases significantly under a small strain change. In the printed Gyroid structure, the lattice walls start bending and further deformation occurs at nearly constant stress level as bending percolates through the material, where the material reaches a long plateau region. When the compression is over 50%, as shown by the black arrow, the folding-stacking of the lattice wall from top to bottom leads to the full densification region with a strong increase in stress. For large compressive deformations, the Gyroid structure printed by the APH ink shows very little lateral expansion. There is almost zero strain in the directions perpendicular to the loading direction once bending occurs. To further test the elastic property of APH Gyroid hydrogel, we also loaded the sample to 30% strain for 100 cycles without stop, and recorded the evolution of stress-strain curves over cycles (see Fig. 4B (b)). Despite slight mechanical softening during the first several cycles (*e.g.*, from the 1st to 10th cycles), the loading-unloading stress-strain curves in the subsequent cycles approach the steady state. In the APH ink, the bio-elastomers maintain elasticity and strength under large deformations, while the ionic crosslinking facilities the dissipation of mechanical energy. Although not as strong as pure thermoplastic PCL polymer, the APH ink and the defined bending deformation are capable of undergoing up to 30% strain over 100 cycles.

For the printed square grid lattice (Fig. 4A(a)), in contrast, macro-cracks tend to propagate from the intersection of the cross-shaped struts due to a 15% compressive strain, as indicated by the red arrow. The stresses were first localized at the cross region which connects the cell nodes, leading to the preferred fracture at the cross nodes under shear force. With the increased compression, multi-cracks propagated
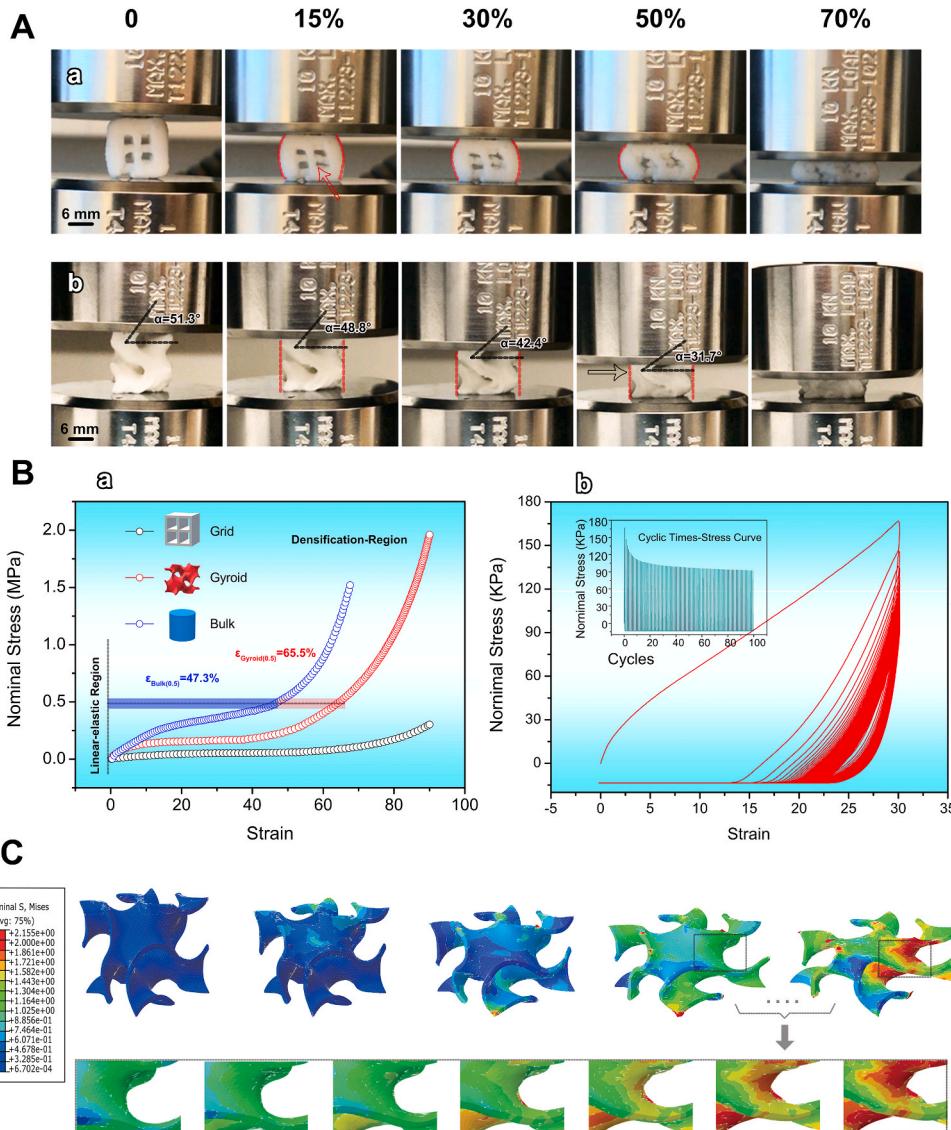
Fig. 4. Mechanical behaviors of the printed samples. A: Photograph series showing the compression of the sample printed with a regular square grid pattern (a) and a Gyroid structure (b), respectively. For large compressive deformations, the Gyroid sample printed by the APH ink shows very little lateral expansion. There is almost zero strain in the directions perpendicular to the loading direction once buckling occurs. B: (a) Normal stress-strain curves of the square grid, Gyroid and bulk structures. Mechanical test of the APH Gyroid sample that was continuously loaded and unloaded to 30% strain for 100 cycles. (b) The stress-strain evolution over cycles. The inset in (b) shows the stress evolution over cycles. C: Numerical simulations of the printed Gyroid unit cell during the compressive deformation. The nominal element stresses are localized at re-entrant regions, which are triggered by the stacking bending behavior.

and expanded rapidly along the stress concentration direction. The sample showed the obvious expansion under axial, compressive stress. The beams bowed out-ward at the center, as outlined by the red dashed line in Fig. 4A(a). When the square grid samples were compressed over 50%, the total collapse of the cell structure gave rise to the integral destruction. For the bulk sample, the stress-strain curve shows steep linear elastic deformation region, leading to large elastic modulus and high plateau strength, compared with the Gyroid and the square grid sample. Different with the Gyroid and square grid, the bulk sample shows the slight hardening response after the elastic region, which extends until the densification region. During the compression process, similar to the square grid, the bulk sample showed expansion behavior along the direction perpendicular to the loading. Multi-cracks were formed to release energy and propagated at the stress concentration zone. Compared with the bulk sample, the Gyroid structure exhibits large compressibility. For example, under the randomly picked nominal stress 0.5 MPa, the bulk sample has 47.3% strain while the Gyroid structure experiences 65.5% strain.

From the stress-strain curves, the energy absorption ability (W) can be calculated by integrating the nominal stress (σ) with respect to strain (ε) up to the densification, that is,

$$W = \int_0^{\varepsilon_D} \sigma \, d\varepsilon \tag{2}$$

From equation (2), we can calculate that $W_{Gyroid} = 1.34 W_{Bulk} = 9.62 W_{Square\ Grid}$. For the compressive modulus ($E = \Delta y_i / \Delta x_i$) of Gyroid and square grid structure, it depends on the stiffness of the materials, and it is found that $E_{Gyroid} = 3.934\ E_{Square\ Grid}$ from our experimental results. Therefore, we can conclude that the Gyroid structure exhibits a larger compressibility and better energy absorbability than the square grid structure. Owing to the large surface-to-volume ratio, the Gyroid sheet-based structure can withstand more stresses because the stresses can distribute over the surface. Such a feature makes the Gyroid sample more effective in carrying the applied load and smooth stress transferring mechanism [25]. Furthermore, the decreased angle α (marked in Fig. 4A(b)) under the compressive load leads to a rotation of the sheet, which infers that the Gyroid sheet deforms as a mixed mode of oriented local stretching and bending during the three different deformation stages [29]. The heterogeneous localized surface tension, resembling the natural ECM, exhibits stress relaxation in response to a deformation, which can promote cell spreading in 3D culture and enhanced osteogenic differentiation [31,32].

For the printed Gyroid sheet-based structure, as mentioned earlier, there is a competition between the forces of air on two sides of a curved wall, which makes the lattices wall prone to yield with the conjoint wall-to-wall contraction or densification. The bending and stacking behaviors, combined with the intrinsic curvature, induce distinct lateral deformation behaviors. To further capture the compressive response of Gyroid structure, we have conducted numerical simulations by commercial finite-element package *Abaqus/Explicit* 2017 (Fig. 4C). From the von Mises stress distribution at different strain level, stresses are first distributed over the surfaces and localized at the curve region that connects the cell nodes. These symmetrical re-entrant walls exhibit plastic deformation, which then triggers the bending stacking behavior layer by layer. The onset and location of plastic strain localization are in good agreement with our observations in the compressive experiment of APH Gyroid structure, which indicates better load bearing capability and stress transferring mechanism.

2.3. Biocompatibility characterization

To demonstrate the biocompatibility of the material, flat APH sheets were seeded with lentiviral-tdTomato transfected human umbilical endothelial cells (HUVEC) to assess their ability to support cell adhesion

and proliferation. Previous works have demonstrated that Alginate and PCL are poor materials for cell attachment and proliferation [17]. The addition of hydroxyapatite and nanoclay endows the rough surface and wettability, which enhance serum protein adsorption and hence provide cells binding site for attachment [33]. By day 3, substantial adhesion and spreading of the HUVECs were observed (Fig. 5A). The cells continued to proliferate over the course of 10 days and occupied the entire scaffold surface, forming microcapillary-like structures. This could positively contribute to scaffold efficacy because tissue vascularization is essential to the integration of tissue implants and their survival in the host. In addition, angiogenesis and vascularization play a crucial role in osteogenesis. The extent of cell proliferation was quantified by counting the number of DAPI-positive cells using ImageJ (Fig. 5B). By day 10, there was statistically significant increase in the number of DAPI-positive cells on the scaffold, indicating that the APH scaffold is biocompatible and able to support cell proliferation. Our 3D-printed gyroid structures also supported HUVEC survival over 14 days (see Fig. S5 in Supplementary Materials).

2.4. Water absorption and affinity

A potential scaffold as implantation for tissue engineering should actively absorb body fluid and nutrient. It is well known that PCL is hydrophobic and does not have any physiological activity when it contacts the living tissue. Jakus et al. [18] significantly improved the water affinity of thermoplastic polymer PCL and PLGA by incorporating 90 wt% HA bioceramic. According to Flory-Rehner theory [34], water absorption and storage capability of crosslinked polymer can be described as the balance between the free energy of hydration and the elastic free energy of polymer matrix. Increasing the number of ionic groups in the polymer matrix can increase the capability of water absorption and storage because the ionic groups provide an additional driving force for water affinity through their large hydration energy. Therefore, we hypothesize that in the APH ink, the successful incorporation of Alginate acid aqueous solution into the hydrophobic polymer matrix would lead to an instant increase in water affinity of printed scaffolds.

To validate the hypothesis, the water absorption and storage capability of APH material was performed in triplicate through the immersing and drying process. Fig. 6A(a) shows the weight variations of samples after immersing into deionized water and subsequently drying at 60 °C. Fig. 6A(b) and (c) present the evolution of water retention of the samples during the immersion and drying processes, respectively. The capability of water absorption and storage is attributed to the availability of a large number of anionic –COOH groups from Alginate, thereby causing the distinct variation in water absorption content. Besides, when saturated with water (as shown in Supplementary Materials Fig. S6), the APH printed scaffold changed the state from floating in the water to sinking at the bottom. The increased density indicates that the pores are fully accessible. This open porous characteristic is highly favorable for nutrient diffusion, cell viability, and osteointegration. The water absorption and retention evaluation of APH printed scaffold could also be triggered by loading (see Supplementary Materials Fig. S7 and Movie S8).

To further characterize the wettability of APH ink, we measured the water contact angle by an automatic microscopic contact angle meter (MCA-3, KYOWA, Japan) as shown in Fig. 6B. The wettability refers to how a liquid deposited on a solid substrate spreads out or the ability of liquids to form contact area with a solid substrate. The larger the wetting tendency is, the smaller the contact angle or the surface tension is. The contact angle (θ) can be defined from the equilibrium of surface tension in the three intersecting phases (γ_{SV}, γ_{SL}, and γ_{LV}) according to the classical Young's equation [35],

$$\cos\theta = \frac{\gamma_{SV} - \gamma_{SL}}{\gamma_{LV}} \tag{3}$$
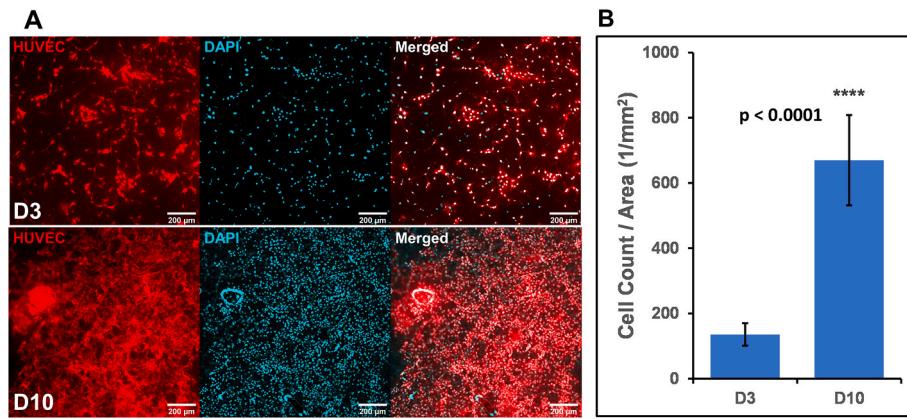
Fig. 5. APH supported cell adhesion and proliferation over 10 days. A: Human umbilical vein endothelial cells (HUVEC) (red, and the nuclear staining with DAPI, blue) adhesion on the APH material. B: The extent of cell proliferation quantified by counting the number of DAPI-positive cells. (For interpretation of the references to colour in this figure legend, the reader is referred to the Web version of this article.)
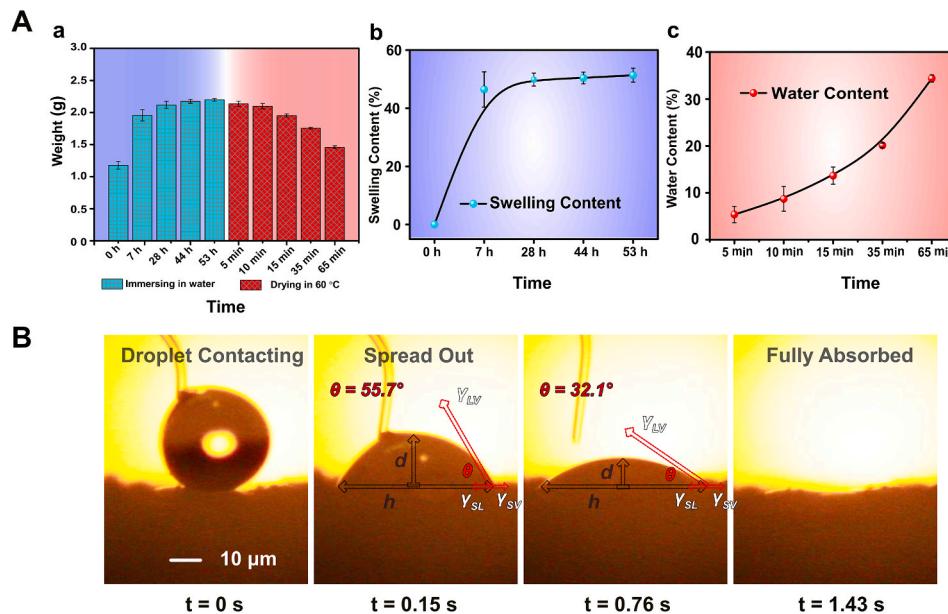
Fig. 6. The water absorption and retention ability of APH scaffolds. A: (a) Weight variations of samples triggered by immersing the sample into the water and subsequently drying at 60 °C. (b) and (c) present the swelling profiles and water contents of the samples during immersing in deionized water and drying at 60 °C, respectively. The water absorption and storage evaluation of APH samples could also be triggered by loading. B: Contact angle measurement for the APH scaffold surface.

where γ_{SV}, γ_{SL}, and γ_{LV} are the surface tension for solid-vapor, solid-liquid and liquid-vapor, respectively. In our experiments, the contact angle (θ) for APH material decreased with time from the value of 55.7° to 32.1°, and water was fully absorbed in 1.43s. As a comparison, in the 3D printed PCL-90 wt%HA and PLGA-90 wt%HA composites system [18], the initial water contact angle is 82°, and waster is absorbed in 6 min. A smaller average contact angle means that a shorter time is needed for the formation of a continuous water film between the adjacent contact substrate. As a result, we confirm the excellent wettability of our sample.

The adhesion energy at steady state (W) could be described as Young-Dupre equation [35]:

$$W = \gamma_{LV} + \gamma_{SV} - \gamma_{SL} \tag{4}$$

When equation (4) is substituted into equation (3), we can obtain:

$$W = \gamma_{LV}(1 + \cos\theta) \tag{5}$$

For water droplet, γ_{LV} is about 72.8 mJ m^{-2} [36]. We can calculate the dynamic adhesion energy of APH material, which is 113.568 mJ m^{-2} when the water droplet is deposited on the substrate for 0.15 s, and

134.68 mJ m^{-2} for 0.76 s. For 3D printed PCL-90 wt%HA and PLGA-90 HA Wt.% composites system [18], the adhesion energy was calculated to be 112.11 mJ m^{-2} when the water droplet is deposited on the substrate for 2 min. The superior water compatibility imparts great hydrophilicity and high liquid absorbency to the APH printed scaffold, which is significant for potentially favorable affinity to the cells and tissues. In addition, the combination of open porous characteristics and the capability of fluid storage and absorption make the printed material ideal for bioactive factors and nutrient infiltration.

3. Conclusion

In summary, we demonstrate a self-supporting hydrogel ink to seamlessly integrate and enhance the mechanical properties and designed functions of DIW scaffolds at room temperature. The printing strategy could be generalized to produce a wide combination of weakly crosslinked nature-origin hydrogel and biomedical thermal-plastic polymers, imparting an integration of mechanical toughness, water absorption and retention capability, and superior 3D printability. To achieve complexity and functional performance of APH scaffolds, we directly in-air print Gyroid meta-structures as well as ear, aortic valve

conduits and hierarchical architectures via a single nozzle. The superior water affinity shows great hydrophilicity and high liquid absorbency in the APH printed structures. Mechanically, the mixed stretching-bending deformation of symmetrical re-entrant cellular lattices and the unique curvature patterns are combined to provide small lateral expansion and large compressive energy absorbance when external forces are applied on the printed Gyroid scaffold. Through *in vitro* studies, APH ink exhibits excellent cells affinity.

Apart from Gyroid, many mechanical meta-structures were designed by a unique combination of the individual strut (bending or stretching) [37,38], and periodical assembly in three independent directions. Moreover, unlike the scaffold with solid non-porous or random porous characteristics [39], the incorporation of porous channels [40] into the Gyroid scaffold may greatly improve vessel infiltration. The interconnected porous characteristics of these meta-structures and a mixed-mode of local stretching and bending are highly desirable for tissue ingrowth in 3D culture. Our work creates an integration of biofunction-structure-mechanical properties, which would expand the applications of 3D direct writing hydrogels in tissue engineering.

CRediT authorship contribution statement

Lei Zhang: Methodology, Investigation, Data curation, Visualization, Formal analysis, Writing – original draft. **Wenhan Lee:** Investigation, Data curation, Visualization, Formal analysis, Writing – original draft. **Xinhao Li:** Investigation. **Yanhui Jiang:** Formal analysis. **Nicholas Xuanlai Fang:** Writing – review & editing. **Guohao Dai:** Conceptualization, Supervision, Resources, Formal analysis, Writing – review & editing. **Yongmin Liu:** Conceptualization, Supervision, Resources, Formal analysis, Writing – review & editing.

Declaration of competing interest

The authors declare that they have no known competing financial interests or personal relationships that could have appeared to influence the work reported in this paper.

Acknowledgement

Appendix A. Supplementary data

Supplementary data to this article can be found online at https://doi.org/10.1016/j.bioactmat.2021.08.015.

References

[1] Q. Feng, K. Wei, K. Zhang, B. Yang, F. Tian, G. Wang, L. Bian, NPG Asia Mater. 10 (2018) e455.
[2] A. De Mori, M. Peña Fernández, G. Blunn, G. Tozzi, M. Roldo, Polymers 10 (2018) 285.
[3] F. Gao, Z. Xu, Q. Liang, B. Liu, H. Li, Y. Wu, Y. Zhang, Z. Lin, M. Wu, C. Ruan, Adv. Funct. Mater. (2018).
[4] P.L. Lewis, R.M. Green, R.N. Shah, Acta Biomater. (2018).
[5] M. Yan, P.L. Lewis, R.N. Shah, Biofabrication (2018).
[6] J.A. Rowley, G. Madlambayan, D.J. Mooney, Biomaterials 20 (1999) 45.
[7] J.A. Hunt, R. Chen, T. van Veen, N. Bryan, J. Mater. Chem. B 2 (2014) 5319.
[8] P. Jiang, C. Yan, Y. Guo, X. Zhang, M. Cai, X. Jia, X. Wang, F. Zhou, Biomater. Sci. 7 (2019) 1805.
[9] A.C. Daly, S.E. Critchley, E.M. Rencsok, D.J. Kelly, Biofabrication 8 (2016), 045002.
[10] J. Radhakrishnan, A. Manigandan, P. Chinnaswamy, A. Subramanian, S. Sethuraman, Biomaterials 162 (2018) 82.
[11] N.A. Chartrain, C.B. Williams, A.R. Whittington, Acta Biomater. 74 (2018) 90.
[12] S.L. Taylor, A.E. Jakus, K.D. Koube, A.J. Ibeh, N.R. Geisendorfer, R.N. Shah, D. C. Dunand, Acta Astronaut. 143 (2018) 1.
[13] T. Xu, K.W. Binder, M.Z. Albanna, D. Dice, W. Zhao, J.J. Yoo, A. Atala, Biofabrication 5 (2012), 015001.
[14] J. Kundu, J.H. Shim, J. Jang, S.W. Kim, D.W. Cho, J. Tissue Eng. Regener. Med. 9 (2015) 1286.
[15] S.U. Maheshwari, V.K. Samuel, N. Nagiah, Ceram. Int. 40 (2014) 8469.
[16] K.W. Boere, J. Visser, H. Seyednejad, S. Rahimian, D. Gawlitta, M.J. Van Steenbergen, W.J. Dhert, W.E. Hennink, T. Vermonden, J. Malda, Acta Biomater. 10 (2014) 2602.
[17] A.C. Daly, F.E. Freeman, T. Gonzalezfernandez, S.E. Critchley, J. Nulty, D.J. Kelly, Adv. Healthcare Mater. (2017) 1700298.
[18] A.E. Jakus, A.L. Rutz, S.W. Jordan, A. Kannan, S.M. Mitchell, C. Yun, K.D. Koube, S. C. Yoo, H.E. Whiteley, C.P. Richter, Sci. Transl. Med. 8 (2016), 358ra127.
[19] A.E. Jakus, E.B. Secor, A.L. Rutz, S.W. Jordan, M.C. Hersam, R.N. Shah, ACS Nano 9 (2015) 4636.
[20] A.E. Jakus, K.D. Koube, N.R. Geisendorfer, R.N. Shah, Sci. Rep. 7 (2017) 44931.
[21] T. Ahlfeld, G. Cidonio, D. Kilian, S. Duin, A. Akkineni, J. Dawson, S. Yang, A. Lode, R. Oreffo, M. Gelinsky, Biofabrication 9 (2017), 034103.
[22] A. Hoppe, N.S. Güldal, A.R. Boccaccini, Biomaterials 32 (2011) 2757.
[23] Y. Liu, H. Meng, S. Konst, R. Sarmiento, R. Rajachar, B.P. Lee, ACS Appl. Mater. Interfaces 6 (2014) 16982.
[24] Q. Gao, X. Niu, L. Shao, L. Zhou, Z. Lin, A. Sun, J. Fu, Z. Chen, J. Hu, Y. Liu, Y. He, Biofabrication 11 (2019), 035006.
[25] O. Al-Ketan, R. Rezgui, R. Rowshan, H. Du, N.X. Fang, R.K. Abu Al-Rub, Adv. Eng. Mater. 20 (2018) 1800029.
[26] S. Khaderi, V. Deshpande, N. Fleck, Int. J. Solid Struct. 51 (2014) 3866.
[27] Z. Qin, G.S. Jung, M.J. Kang, M.J. Buehler, Sci. Adv. 3 (2017), e1601536.
[28] S.C. Han, J.M. Choi, G. Liu, K. Kang, Sci. Rep. 7 (2017) 13405.
[29] A. Ataee, Y. Li, M. Brandt, C. Wen, Acta Mater. 158 (2018) 354.
[30] H.H. Tønnesen, J. Karlsen, Drug Dev. Ind. Pharm. 28 (2002) 621.
[31] O. Chaudhuri, L. Gu, D. Klumpers, M. Darnell, S.A. Bencherif, J.C. Weaver, N. Huebsch, H-p Lee, E. Lippens, G.N. Duda, Nat. Mater. 15 (2016) 326.
[32] J. Lou, R. Stowers, S. Nam, Y. Xia, O. Chaudhuri, Biomaterials 154 (2018) 213.
[33] D.D. Deligianni, N.D. Katsala, P.G. Koutsoukos, Y.F. Missirlis, Biomaterials 22 (2000) 87.
[34] G.M. Geise, D.R. Paul, B.D. Freeman, Prog. Polym. Sci. 39 (2014) 1.
[35] M.E. Schrader, Langmuir 11 (1995) 3585.
[36] W.D. Harkins, F. Brown, J. Am. Chem. Soc. 41 (1919) 499.
[37] X. Zheng, H. Lee, T.H. Weisgraber, M. Shusteff, J. Deotte, E.B. Duoss, J.D. Kuntz, M.M. Biener, Q. Ge, J.A. Jackson, Science 344 (2014) 1373.
[38] T.A. Schaedler, A.J. Jacobsen, A. Torrents, A.E. Sorensen, J. Lian, J.R. Greer, L. Valdevit, W.B. Carter, Science 334 (2011) 962.
[39] J. Liu, G. Chen, H. Xu, K. Hu, J. Sun, M. Liu, F. Zhang, N. Gu, NPG Asia Mater. 10 (2018) 827.
[40] O. Al-Ketan, R.K.A. Al-Rub, R. Rowshan, Advanced Materials Technologies 2 (2017) 1600235.